Tailoring Molecular Space to Navigate Phase Complexity in Cs-based Quasi-2D Perovskites via Gated-Gaussian-Driven High-Throughput Discovery

Minsub Um[1,‡], Sheryl L Sanchez[2,‡], Hochan Song[3,‡], , Benjamin J. Lawrie[4,5], Hyungju Ahn[6], Sergei V. Kalinin[2], Yongtao Liu[4], Hyosung Choi[3]*, Jonghee Yang[1]*, Mahshid Ahmadi[2]**

[1] *Department of Chemistry, Yonsei University, Seoul 03722, Republic of Korea.*

[2] *Institute for Advanced Materials and Manufacturing, Department of Materials Science and Engineering, The University of Tennessee, Knoxville, TN 37996, United States.*

[3] *Department of Chemistry, Research Institute for Natural Sciences and Research Institute for Convergence of Basic Science, Hanyang University, Seoul 04763, Republic of Korea.*

[4] *Center for Nanophase Materials Sciences, Oak Ridge National Laboratory, Oak Ridge, TN 37831, United States.*

[5] *Materials Science and Technology Division, Oak Ridge National Laboratory, Oak Ridge, TN 37831, United States.*

[6] *Pohang Accelerator Laboratory, POSTECH, Pohang 37673, Republic of Korea.*

[‡] *These authors contributed equally*

Corresponding Authors

Mahshid Ahmadi (E-mail: mahmadi3@utk.edu)

Jonghee Yang (E-mail: jhyang@yonsei.ac.kr)

Hyosung Choi (E-mail: hschoi202@hanyang.ac.kr)

Yongtao Liu (E-mail: liuy3@ornl.gov)

Abstract

Cesium-based quasi-two-dimensional (2D) halide perovskites (HPs) offer promising functionalities and low-temperature manufacturability, which are suited to stable tandem photovoltaics (PVs). However, the chemical interplays between the molecular spacers and the inorganic building blocks during crystallization cause substantial phase complexities in the resulting matrices. To successfully optimize and implement the quasi-2D HP functionalities, a systematic understanding of spacer chemistry, along with the seamless navigation of the inherently discrete molecular space, is necessary. Herein, by utilizing high-throughput automated experimentation, the phase complexities in the molecular space of quasi-2D HP films are explored, thus identifying the chemical roles of the spacer cations on the synthesis and functionalities of the complex materials. Furthermore, we introduce a novel active machine learning algorithm leveraging a two-stage decision-making process, called gated Gaussian process Bayesian optimization (Gated-GPBO), to navigate the discrete ternary chemical space defined with two distinctive spacer molecules, 1,4-butanediammonium and phenethylammonium. Through simultaneous optimization of photoluminescence intensity and stability of quasi-2D HPs which 'tailors' the chemistry in the molecular space, a ternary-compositional quasi-2D HP film realizing excellent optoelectronic functionalities, as well as the high PV performance is demonstrated. This work not only provides a pathway for the rational and bespoke design of complex HP materials but also sets the stage for accelerated materials discovery in other multifunctional systems.

Introduction

Halide perovskites (HPs) are now leading materials pioneering photovoltaic (PV) technologies, owing to their simple solution processibility and excellent optoelectronic functionality. Among them, inorganic Cs-based HPs, where volatile methylammonium is excluded, are anticipated to be advantageous to thermal stability. Also, it offers a relatively wide bandgap of ~1.7-1.8 eV that is desired for front cell in tandem PV applications[1-4], while excluding substantial bromine incorporation that compromises bandgap stability via halide segregation[5, 6]. However, thermodynamically, the synthesis of photoactive α-$CsPbI_3$ phase requires high temperatures over 325 ^oC[7, 8]. Such high temperature is incompatible with the organic-based hole-transport materials (HTMs), thereby realizing p-i-n type PVs – chemically more stable and a conventional architecture for tandem PV application – difficult.

Dimensional confinement of HP lattices via surface coordination of large molecular spacers allows for the formation of distinctive 2D HP structures with various unit thicknesses of inorganic octahedra sheets (described as *n*), called quasi-2D HPs. The quasi-2D HPs offer more thermodynamically feasible synthesizability, enabling crystallization at relatively lower temperatures while not compromising the overall bandgap of the materials system with respect to 3D counterparts[9-11]. Furthermore, the molecular spacers coordinated to the quasi-2D HP surface improve the stability of the HP lattices, as it can act as a protection layer against environmental stressors (e.g., oxygen and moisture)[12-14].

A crucial challenge to fully exploit the quasi-2D HPs to optoelectronic applications lies in the concurrent emergence of multiple quasi-2D HP phases and their spatial distributions in the synthesized film matrices. Primarily, this is caused by adopting the nonequilibrium fabrication processing, though it is optimally compatible with manifesting a fairly homogeneous 3D HP matrix[15-17]. But more importantly, profound chemical interactions among the spacer cations, inorganic building blocks, and even solvents can manifest different crystallization dynamics and/or energetic pathways for each phase[18-23]. Thus, a comprehensive understanding of the supramolecular interaction is vital for resolving such phase complexities in quasi-2D HPs, thereby realizing bespoke manipulation and subsequent utilization of the complex materials for optoelectronic applications.

In fact, the chemical variability of spacer cations offers an infinite molecular space, making the systematic and comprehensive investigation of the supramolecular interaction difficult. Particularly, due to the coexistence and interplays of multiple physicochemical parameters of molecular spacer affecting HP crystallizations, manual exploration to resolve such a multi-faceted problem is extremely challenging. Moreover, the chemistry in the vast molecular spaces is – inherently – discrete, rather than continuous landscapes. Thus, for optimizing the optoelectronic functionalities of the quasi-2D HPs, seamless navigation of such intricate chemical space is necessary, which is also difficult based on the classical, single-directional process refinement techniques.

Instead, extensive efforts to the quasi-2D HPs have been focused on utilizing them towards optoelectronic applications, particularly prioritizing the development of high-performance and stable devices. Thus, the exploration of the genuine roles of spacer cations in the materials system remains elusive so far. That is, a legitimate consensus on selecting optimal spacers and/or chemical compositions, as well as the fundamental insights into designing functional materials are still lacking.

In this work, we employ a high-throughput automated experimental workflow to effectively explore the chemical space associated with phase complexities, including phase emergence behaviors, in quasi-2D HP films[13, 14, 24-29], defined by the spacer cations Here, five primitive 2D HP systems employing spacer molecules with distinctive physicochemical properties are selected: *n*-butylammonium (BA), butane-1,4-diammonium (BDA), thiopheneethylammonium (ThEA), and 3,3-diphenylpropylammonium (DPA), respectively; these cations represent key aspects in the chemical space – including molecular sizes, shapes, molecular weights and dipole moments – of the molecules. By combinatorial mixing them with 3D $CsPbI_3$, the spacer-dependent phase emergence behaviors and stability of the low-temperature (<100 ^oC) processed film matrices are systematically assessed.

Multiple features strongly associated with the chemistry of spacer cations were identified. It is found that the use of a spacer with phenyl rings manifests stable 3D-like phases – high-*n* 2D HP structures where the surface coordinated spacers protect 3D $CsPbI_3$ lattice, which is failed to realize by employing thiophene ring or short alkyl chain spacers. This allows for the construction of stable HP film matrices that render an optimal bandgap of ~1.8 eV. Such discrepancy is likely attributed to the difference in geometric symmetry for spacer-precursor chemical interaction. Note that the HP matrix with bulky DPA offers uneven surface morphology with segmented 3D-like HP crystallites compromising charge transport upon device application, though it exhibits outstanding phase stability[16, 30]. Additionally, in contrast to the Ruddlesden-Popper (RP) type HPs that typically render severe 2D/3D phase separation along the vertical direction[31, 32], incorporation of Dion-Jacobson (DJ) type perovskite (i.e., $BDAPbI_4$) homogenizes the vertical phase distributions. These observations collectively reveal the importance of spacer chemistry for synthesizing quasi-2D HP matrices.

Inspired by the comprehensive observations via high-throughput experimentation, it is envisaged that a new quasi-2D HP matrix deploying benefits of each binary system can be designed via compositional mixing of both RP- and DJ-type 2D HP endmembers (i.e., PEA_2PbI_4 and $BDAPbI_4$, respectively) in a ternary system. Here, by developing and deploying a gated Gaussian process Bayesian optimization (Gated-GPBO), we navigate chemistry in such intricate and discrete molecular space and identify optimal compositions offering ideal bandgap with minimized phase inhomogeneities and local phase distributions. Indeed, the p-i-n type PVs employing the quasi-2D HP film – tailored by Gated-GPBO – exhibit improved performances than those deduced by grid-search, thus effectively identifying optimal compositions directed to device-applicable films at the low-temperature fabrication process. This clearly shows the powerfulness of the Gated-GPBO for the exploration of complex materials systems. Collectively, this work provides a new research workflow not only

uncovering fundamental insights into the complex quasi-2D HP system but also presenting designing principles for bespoke materials design and functionality manipulations towards sustainable applications.

Results and Discussions

Exploration of Spacer-Dependent Phase Emergence Behaviors in Quasi-2D HPs

Differences in molecular structure bestow different chemical properties on the spacer cations. For the synthesis of quasi-2D HPs, this in turn manifests notable differences in chemical interactions with other neighboring chemical species, which profoundly tunes the crystallization behaviors, stability and other functionalities of the matrices. While the control over such behaviors is crucial for designing functional materials, understanding such multi-dimensional properties in the complex materials system merely with classical batch-type investigation workflow falls short of the efficiency and insight needed for advanced material design. Specifically, such manual exploration requires a long and intricate exploration loop, as well as expensive costs. Thus, the progress is deemed to be slow, highly attributed to the difficulty in accurate decision making from limited information at each stage[33].

To systematically explore the spacer-dependent phase emergence behaviors in the corresponding quasi-2D HPs, we utilize a high-throughput automated experimental workflow[14, 27, 29]. Our designed workflow allows maximal acceleration of the synthesis-characterization-analysis cycle with much cheaper costs, enabled by the incorporation of rapid characterization methods and easy to interpret ML methods in the discovery loop. Here, the precursor solutions with different 2D:3D composition ratios – prepared via combinatorial mixing of 3D $CsPbI_3$ and respective 2D HP precursors, as shown in **Figure S1** – are drop-casted onto the glass substrates. Subsequent thermal annealing at 95 ^oC allows for the synthesis of quasi-2D HP film arrays with the respective spacer cations. The resulting film arrays are quickly transferred to an optical reader to collect photoluminescence spectra from both the top and bottom surfaces over time. This allows us to identify the distinct phase emergence behaviors and vertical phase inhomogeneities, and assess their stabilities in each quasi-2D HP combinatorial library (**Figure 1a**). Here, we select five representative spacer cations as precursors: BA, BDA, ThEA, PEA, and DPA. In contrast to BA with a short alkyl chain, PEA, ThEA and DPA have one or two aromatic rings in the corresponding molecular structures, allowing for understanding the role of aromatic rings in phase emergence behaviors and stabilities; ThEA and DPA respectively provide additional insights into the chemical impact of heterocycle and the number of the aromatic ring on the phase growth of quasi-2D HPs. Also, BDA represents the phase growth features of DJ-type perovskite.

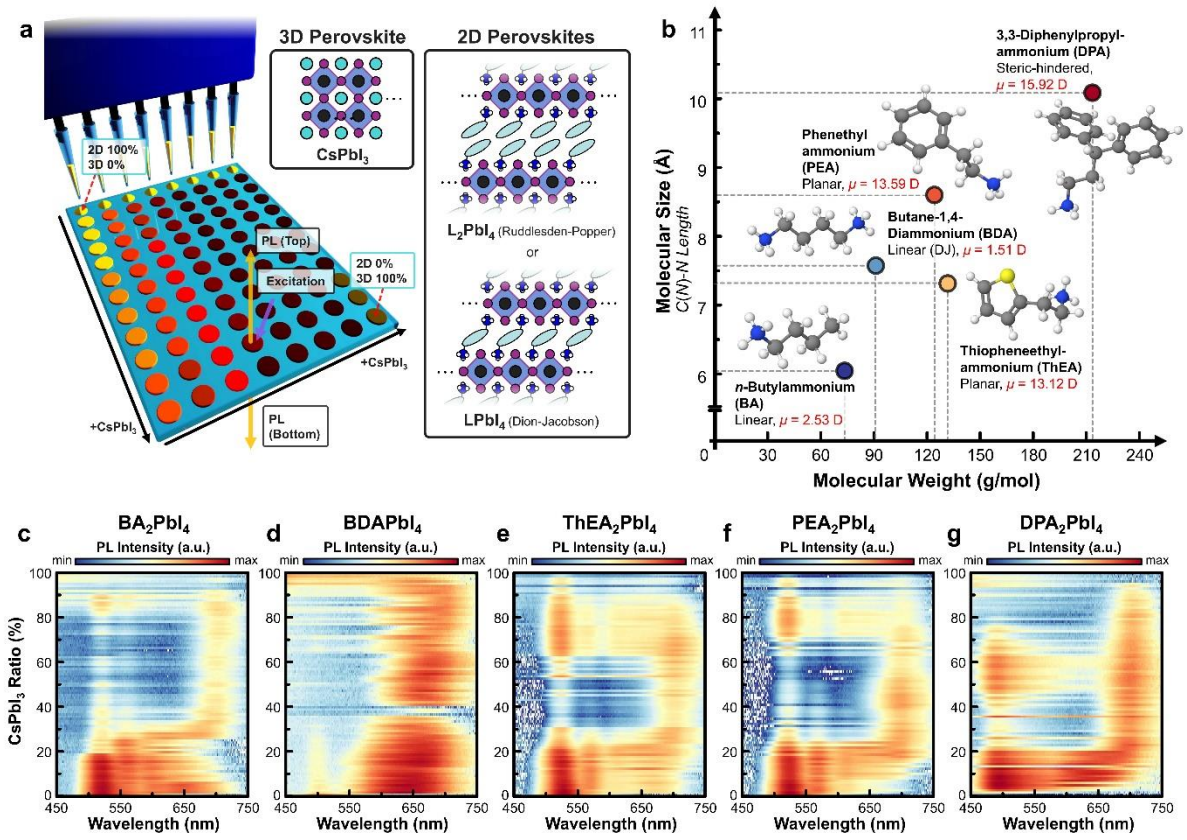

Figure 1. (a) Schematic illustrating a high-throughput automated synthesis of quasi-2D HP film arrays with a pipetting-robot system. (b) A chemical space of molecular spacers in this study. (c-g) Composition-dependent top-surface PL spectra of the quasi-2D HP films having different spacer cations, showing differences in phase emergence behaviors: (c) BA, (d) BDA, (e) ThEA, (f) PEA, and (g) DPA, respectively.

Figure 1c-g exhibit the initial top-emitting PL spectra of the quasi-2D HP films as a function of 3D $CsPbI_3$ composition ratios with different 2D HP endmembers, clearly visualizing the differences in phase emergence behaviors along the combinatorial libraries (the photographs of the corresponding film arrays and the entire datasets of time-evolved PL spectra for each combinatorial library are shown in Figure S2 and **Figure S3-S7**, respectively). In contrast to 100% 3D $CsPbI_3$ film, where the non-perovskite yellow phase dominantly emerges, the incorporation of 2D HP endmember manifests the growths of 2D or 3D-like HP phases involving the corresponding PL spectra. For all cases, in addition to the *n*=1 2D phase that exclusively formed at 0% – evidenced by the single PL peak centered at ~510-520 nm, PL spectra of the higher-*n* 2D phases emerge with increasing the 3D $CsPbI_3$ composition ratios. However, the trends in phase emergence behaviors show distinctive features depending on the selection of spacer cation.

We first explore the phase emergence behavior of the BA-based quasi-2D HPs – a RP-type spacer with a short alkyl chain (**Figure 1c**). At low 3D ratios (<10%), in addition to the dominant emergence of low-*n* 2D HPs (e.g., *n*=1-3; PL peaks <600 nm),

considerable PL signals ranging 600-700nm associated with high-*n* phases (e.g., *n*≥4) are observed, though their synthesizability are comparatively unfavorable in thermodynamics than that of the low-*n* counterparts[10, 11]. Presumably, these high-*n* HPs are kinetic products, given the low molecular weight of BA and the lower emergences of such phases in other combinatorial libraries with ThEA and PEA spacers at this compositional range (*vide infra*); it is likely attributed to the higher diffusivity of BA in the precursor system and lower degree of inter-molecular interaction than other spacer cations. Note that, further increases in the 3D ratio (up to ~25%) counterintuitively suppress the crystallization of the high-*n* HPs that require 3D HP building blocks, again corroborating that the emergence of these phases is thermodynamically unfavorable in such compositional range.

With increasing 3D ratio from 25 to 35%, a progressive emergence of higher-*n* HPs is observed, and over ~35%, a distinct phase emergence behavior consisting of 3D-like phases (centered at ~700 nm), involving marginal *n*=1 and 2 2D HPs, is observed. Such phase emergence features are consistently observed up to ~90% 3D ratio. These observations indicate that, in this composition range, the BA-based 3D-like HP structures can be synthesized at a low annealing temperature (95^{o}C). We see inappreciable emission intensity for the compositions with over 90% 3D ratio, suggesting that thermodynamically favored non-perovskite δ-$CsPbI_3$ crystallites, rather than 3D-like HPs, are formed. This also implies that sufficient amounts of spacer cation are vital for overcoming the thermodynamics in making 3D-like HP crystallites at such a low annealing temperature.

Note that, after 10 hours, the PL peak intensities of the *n*=1 and 2 2D HPs are increased at the expense of those from the 3D-like phases across the compositional space (**Figure S8a**). The decreased PL intensity of the 3D-like HPs indicates the temporal degradation of the corresponding crystallites upon ambient exposure during the measurements. The degradation action disintegrates the 3D-like HPs into fragmented building blocks, which are, in turn, merged into *n*=1 and 2 2D phases. That is, BA offers insufficient ambient stability of the 3D-like HPs, which makes them impractical for PV applications. Essentially, these changes are associated with the degradation action of the quasi-2D HPs, and thus, it is legitimate to assume that such spectral features showing across the quasi-2D HP compositional space are an indicative of the functionality of the spacer cation on the stability of the film matrices; the appreciable spectral changes in the compositional space indicates that the corresponding spacer cation cannot benefit the stability of the quasi-2D HP films.

In contrast, DJ-spacer, BDA, exhibit different phase emergence behaviors. It is found that multiple 2D HP phases with *n*≥3 thicknesses emerge in the film matrix at the low 3D ratios, which separate from the *n*=1 2D HP (**Figure 1d**). These 2D HPs (e.g., *n*≥3) render a broad PL band ranging in 550-700 nm wavelength. The broadband PL becomes narrower with increasing the 3D ratio up to ~ 35%, which then gradually converge as a strong PL band ranging in 600-700 nm wavelength. Such trends were consistent with further increasing the 3D ratio up to 90%. Note that, in the overall compositional range, the peak position of the broadband PL peak constantly locates

at the lower wavelengths than that of α-$CsPbI_3$ (centered at ~700-710 nm) or 3D-like HP seen in BA counterpart. This suggests that, comparatively, the high-*n* HP phases constructed in BDA-based quasi-2D HP system are thinner than those in the system with RP spacers. We also note that the intensity of the broadband PL is even stronger than those of *n*=1 and 2 2D HPs. That is, BDA tends to manifest higher-*n* phases rather than intermediate 2D phases (e.g., *n*=2-4 2D HPs), allowing efficient charge transport through the non-confined HP lattices[34] – beneficial to PV applications. However, distinct emergences of lower-*n* 2D HPs are observed across the compositional space after 10 hours (**Figure S8b**), suggesting that BDA cannot bestow sufficient phase stability to the quasi-2D HP lattices.

The phase emergence behaviors in the aromatic RP spacers are also explored. ThEA and PEA exhibit similar phase emergence behaviors across compositional space, likely due to their similarity in molecular structure (**Figure 1e and 1f**, respectively). At low 3D ratios up to ~10%, *n*=1 and 2 2D HPs dominantly emerge in both systems. Meanwhile, weak PL signals associated with higher-*n* phases (*n*≥3) are also observed in the synthesized films. Comparatively, the PL emergences of these higher-*n* phases in both quasi-2D HP systems are weaker than those in the BA counterpart. Such discrepancy in the emergence of higher-*n* phases can be synergistically attributed to the heavier molecular weights of ThEA and PEA compared with BA, as well as the stronger inter-molecular interaction between the spacer cations through the aromatic rings in these molecules. The non-trivial π-π stacking behavior, together with their larger molar masses than that of BA, likely impedes the diffusion action in the precursor solution, thus restricting the formation of the kinetic products. Note that the emergence of high-*n* 2D HPs are more suppressed in PEA-based system compared to the ThEA counterpart, despite relatively lighter molecular weight of PEA. This suggest that inter-molecular interaction – particularly, the π-π stacking behavior – of PEA is stronger than that of ThEA.

In both systems, with further increasing the 3D ratios up to ~ 20%, much higher-*n* phases progressively emerge, and then the 3D-like HP phases become dominant when the 3D ratio exceeds ~30% (~25% for PEA), involving marginal amounts of low-n 2D HPs. Similar phase emergence behaviors are also observed in BA-based system, which, however, starts at relatively higher 3D composition ratios of ~40%. This can also be explained by the retarded diffusion of the ThEA and PEA spacers. This subsequently slows down their surface coordination to the HP lattice, and such slower crystallization kinetics offers longer times for growth of inorganic lattice, thus manifesting thicker HPs. Similar crystallization mechanisms have been proposed for the quasi-2D HPs incorporating coordinative molecular additives in the precursor system (e.g., crown ethers, and so on), where their strong coordination actions to the inorganic lattice prevent the complete formation of 2D HPs[35-38].

Over the 3D ratio of ~60%, the intermediate-*n* (e.g., *n*=3-5), as well as the *n*=1 2D phases start to emerge, at the expense of the 3D-like HPs. This suggests that the formation of 3D-like HP phases are no longer to be favorable over this composition ratio. Essentially, this seems to be counterintuitive to the conventional perovskite chemistry, where, stoichiometrically, higher-*n* HP phases are deemed to be emerged

when the 3D composition ratio becomes dominant in the system. In fact, analogous phase emergence features were observed in formamidinium (FA)-based quasi-2D HPs[14], hypothesizing that thermodynamically favorable δ-$FAPbI_3$ phase can disturb the growth of 3D-like phases at such high 3D composition ratios. Considering this, the observed scenarios in this study can also be associated with the formation of thermodynamically favorable δ-$CsPbI_3$ phase.

Temporal stability of the quasi-2D HP phases in ThEA- and PEA-based systems, after exposing the films for 10 hours in ambient atmosphere, are also assessed (**Figure S8c and d**). Appreciable intermediate-*n* 2D HPs emerge in the ThEA-based quasi-2D HP composition space, at the expense of the 3D-like phase. In contrast, marginal changes in phase emergence behaviors are observed across the compositional space of the PEA-based system. These observations imply that PEA cation offers better phase stability compared to ThEA. It is known that PEA in quasi-2D HPs enhances phase stability, as the phenyl ring can protect the inorganic lattice against external stimuli such as O_2 and H_2O[12, 30]. Considering this, the poor stability of ThEA-based quasi-2D HP is likely associated with the heterocyclic structure of thiophene; this can offer a different scenario in chemical interactions which cannot benefit the stability of the HP lattice.

Next, we examined the effect of a larger bulky spacer having two phenyl rings. DPA renders completely different phase emergence features in quasi-2D HPs compared with other systems (**Figure 1g**). It should be noted that pure DPA_2PbI_4 cannot be crystallized unless a minute concentration of 3D $CsPbI_3$ (at least 2 mol.%) is incorporated in the precursor state. With a small amount of 3D precursors, crystallization occurs, producing yellow-colored films exhibiting distinctive asymmetric PL spectra peaked at ~490 nm. Such an unconventional HP crystallization feature and PL behaviors are likely due to the steric hindrance of DPA caused by the proximity of the neighboring phenyl rings at the 2D HP surface[28].

Similar to other RP-type systems, the progressive emergences of intermediate-to-high-*n* phases are also observed in DPA-based quasi-2D HP compositional space, where such features are manifested at even lower 3D ratios – from ~10% to 25% – than the PEA counterparts. The heavier molecular weight of DPA than ThEA or PEA further slows down the diffusion of the spacer in the solution, which thereby attributes to the results. From the 3D ratio of 30 to 90%, the 3D-like phases becomes dominant, which also involves considerable *n*=1 2D phase. Note that, after 10 hours under ambient condition, though the PL intensity of the intermediate-n phases are slightly enhanced at the low 3D ratios (<20%), overall, no appreciable changes in the spectral features across the compositional space is observed (**Figure S8e**). This indicates that DPA spacer manifests excellent stability of the HP lattices, as the two phenyl rings in the molecule can effectively shield the HP lattices from the oxidative species[16, 30].

Having explored the phase emergence behaviors at the top surfaces, we assess the phase emergence behaviors at the bottom-surface to investigate the vertical phase homogeneities in each quasi-2D HP combinatorial library (**Figure S9**) – a key factor determining optoelectronic functionalities. For RP-type HP systems, it is known that,

in contrast to the top surfaces where 3D-like phases are abundant, the low-*n* (e.g., *n*=1 and 2) 2D phases are dominant at the bottom of the matrices (Figure **S9a, c-e**). This is likely due to the imbalanced crystallization kinetics of each HP phase, where the crystallization of the 3D-like HP phase majorly takes place at the solution-air interface initially[31, 32]. The precursor ions of (quasi-)2D HPs reside longer time in the solution and are concentrated at the bottom surface, rather than crystallizing at the top surface – attributed to the stronger solvent-solute interactions due to the larger polarity of the spacer cations[13, 39], which thereby undergo crystallization. Such distinct phase inhomogeneity along the vertical direction can hamper appropriate charge transport, thus significantly restricting the PV performance. In contrast, for Cs-BDA quasi-2D HPs – a representative DJ-type HP system in this study, similar phase emergence behaviors are observed at both the top and bottom surfaces (**Figure S9b**). This suggest that a more homogenized phase distributions are manifested along the vertical direction of the DJ-based quasi-2d HP film matrices, rendering a smoother energetic landscape that allows more efficient vertical charge transport in PV applications. Note that such a difference also implies that the crystallization mechanism of DJ-based quasi-2d HPs does not follow that of RP-type counterparts.

Summarizing, for all quasi-2D HP systems, high-*n* phases emerge with increasing 3D composition ratios. For RP-type systems, higher-*n* or 3D-like phases emerge at the top surface when the heavier spacer cation is employed, which simultaneously suppresses the growth of low-*n* 2D HP kinetic products (e.g. *n*=2-4). In contrast, *n*=1 and/or 2 2D HPs are dominant at the bottom of the film matrices. DJ-type spacer BDA homogenizes the 2D phases along the vertical direction. However, it also manifests thinner 3D-like phases with broader thickness distributions, offering a larger bandgap with energetic inhomogeneities that impede efficient charge transport upon PV applications.

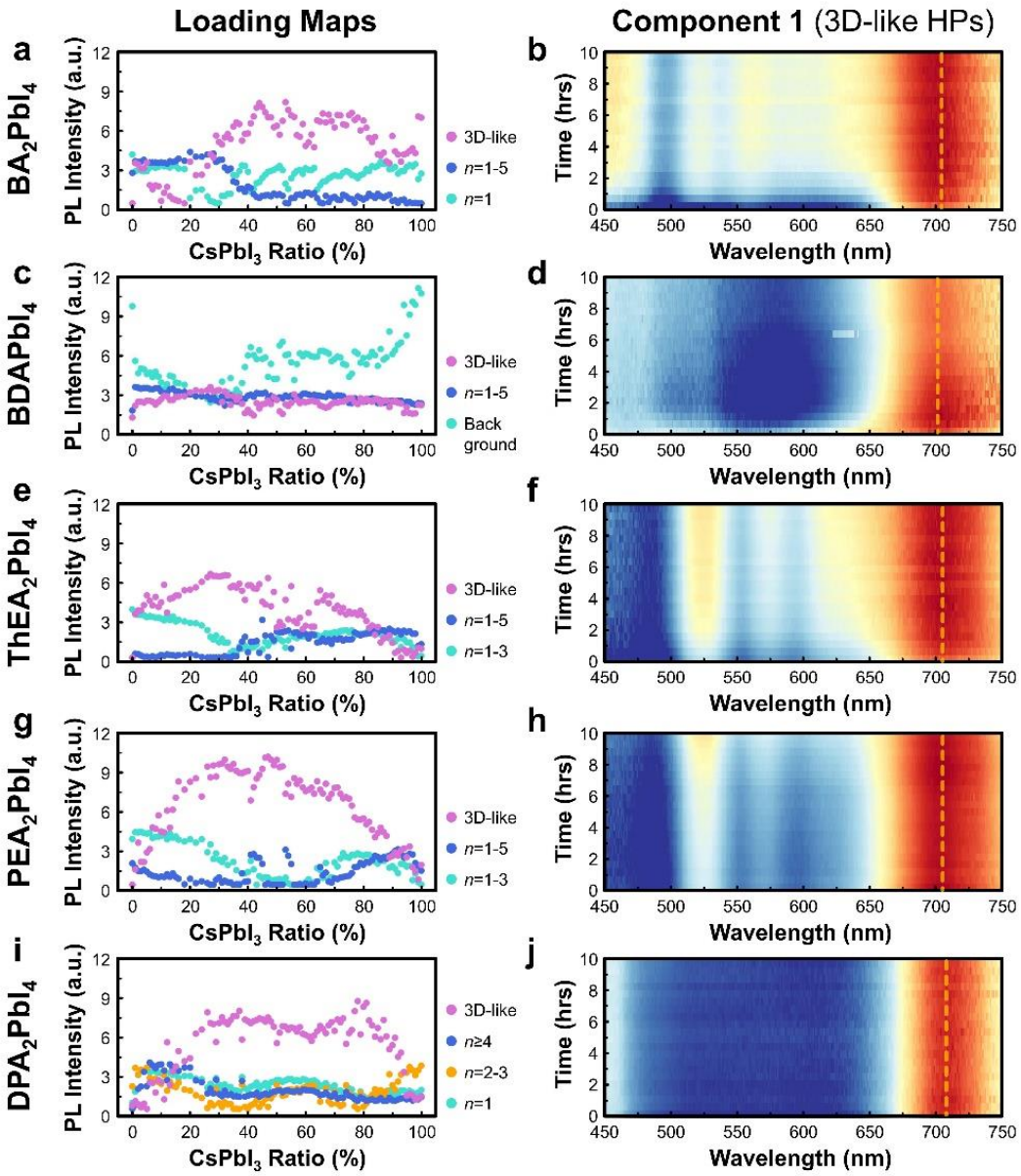

Figure 2. NMF-deconvoluted (a,c,e,g,i) loading maps and (b,d,f,h,j) PL components corresponding to 3D-like HP phases, from the top-emitting PL spectra for the combinatorial libraries of quasi-2D HP films with different spacer cations: (a,b) BA, (c,d) BDA, (e,f) ThEA, (g,h) PEA, and (i,j) DPA, respectively.

To better understand the global trends in the spacer-dependent phase emergence behaviors across compositional space, we utilize non-negative matrix factorization (NMF), an unsupervised machine learning (ML) approach. This multivariate data analysis has been successfully implemented to explore the large chemical space in the quasi-2D HPs, which effectively identifies key features associated with complex materials systems[13, 14, 27]. Through NMF deconvolutions, time-evolutions of key PL features – reflecting the corresponding HP phases – and their composition dependencies (both at the top and bottom surfaces) are identified. This allows us to

visualize the qualitative phase diagrams in each combinatorial library. **Figure 2** and **S10** reveal the key phase emergence behaviors at the top surface of each combinatorial library. Here, we used three components (four for DPA-based system) as an optimal number for NMF analysis, which can reasonably deconvolute the PL datasets.

Through NMF, we first examine the phase emergence behaviors in the BA-based quasi-2D HP system, having a short aliphatic chain and light molecular weight. At the top surface, it is found that low-*n* 2D HPs – particularly, *n*=1 – emerge across the whole compositional range (Component 2; **Figure 2a** and **Figure S10a**). Additionally, a very weak PL peak centered at ~710 nm emerges– assigned to be α-$CsPbI_3$ having a redshifted PL from the that of the 3D-like HPs, which quickly disappears within an hour (**Figure S9a**). This indicates that the α-$CsPbI_3$ HP phase, with a cubic lattice structure, initially forms at the low annealing temperature, which is then quickly disintegrate or transform to other phases due to its intrinsic thermodynamic instability. Note that such a feature cannot be recognized by manual exploration of the PL spectra (**Figure S3-S7**), showing the effectiveness of NMF technique on studying such large datasets. Also, multiple low-*n* HPs (e.g., *n*=1-5) prominently emerge up to 30% of $CsPbI_3$, which are then suppressed at the higher composition ratios (Component 3 in Figure 10a) – as seen in the corresponding PL spectra as a function of 3D ratios **Figure 1c**. Meanwhile, the PL of the 3D-like phases – centered at ~700 nm – starts to emerge over 3D ratios over 40% (**Figure 2b**), suggesting that 3D-like phases start to develop. In contrast, for the case of BDA, with an additional ammonium head in the structure of the spacer molecule, multiple low-*n* HP phases (*n*=1-5), as well as the 3D-like phases emerge across the entire compositional range (**Figure 2c,d** and **Figure S10b**). It is found that the PL intensity of the latter phases gradually decreases over time, attributed to their poor stability. Note that the spectral signature of the emergence of α-$CsPbI_3$ HP is not observed in this system, implying that BDA cannot manifest the construction of the cubic HP lattice.

NMF-deconvolution reveals the similarity in global phase emergence behaviors between ThEA- and PEA-based quasi-2D HP systems (**Figure 2e-h** and **S10c,d**). Qualitatively, the deconvoluted PL features are also analogous to those in the BA-based system, rather than the BDA counterpart, indicating that the type of the spacer cations primarily determines the overall phase emergence behaviors. In both cases, at the top surface, *n*=1 and other low-*n* 2D HPs emerge at low-3D composition ratios, which are gradually suppressed up to the 3D ratio of 40% (Component 2 in **Figure S10c S10d**, respectively). Above 40% and 60% for the ThEA- and PEA-based systems, respectively, these phases start to emerge again and then disappear over 90% 3D ratio. In both cases, NMF deconvolution captures the transient emergence of the *α*-$CsPbI_3$ HP (Component 3), which survives longer times than that observed in the BA counterpart. This implies that the aromatic rings can provide better stability to the HP lattices.

It is worth to note that, particularly for the PEA-based system, there is a specific 3D composition range of 40-60%, where the emergence of 3D-like phases becomes

dominant while the other phases are greatly suppressed or are at the nominal level (**Figure 2g and 2h**). A similar trend was observed in the PEA-formamidinium (FA) quasi-2D HP systems; it was confirmed that vertically aligned 3D-like phases exclusively emerge at this compositional range, expected to benefit PV performances[14].

For DPA-based quasi-2D HPs (**Figure 2i and Figure S10e**), *n*=1-5 2D phases (components 2-4 in **Figure S10e**) concurrently emerge with a similar trend across the entire compositional range, particularly prominent at low 3D concentrations (<30%). The stable 3D-like HPs emerge at a large compositional range of 20-85%. These observations imply that the formation of low-*n* 2D phases is much more restricted than those in ThEA and PEA-based counterparts. Note that the PL peak of the 3D-like HPs exhibits an almost identical PL center to that of *α*-$CsPbI_3$ HP (Component 2), suggesting that the 3D-like phase in DPA-based quasi-2D HP has thick inorganic lattices in the HP lattices (i.e., very high *n* values) on par with those in bulk 3D $CsPbI_3$ HPs[40]. Presumably, the incomplete surface coverage of DPA, as a result of steric hindrance[28], provides appropriate strain to the inorganic lattice to manifest the cubic *α*-$CsPbI_3$ HP phase, which cannot be achieved by using the conventional spacer cations.

The observed correlations between the phase emergence behaviors and the selection of spacers collectively infer distinctive principles for designing quasi-2D HP matrices. In general, heavy molecular spacers manifest the growth of high-*n* or 3D-like HP phases, which are also more stable than the pure 3D $CsPbI_3$ counterpart and therefore benefit PV applications. However, at the same time, this simultaneously causes the strong emergence of low-*n* (particularly, *n*=1) 2D HPs at the bottom, which act as an energetic barrier for charge transport. The DJ-type spacer can greatly mitigate such vertical phase inhomogeneity, although this adversely compromises the phase stability. While the spacers having aromatic rings offer better stability to the 3D-like phases compared to the aliphatic chain, practically, the phenyl ring is more advantageous to phase stability than other heterocyclic rings.

By using NMF analysis, the phase emergence behaviors at the bottom surface of the films are also examined (**Figure S11**). As observed from composition-dependent PL spectra (**Figure S9**), the RP-type quasi-2D HP systems exhibit the dominance of the low-*n* (*n*=1 and 2) 2D phases across the entire compositional range. These 2D HPs have larger bandgaps than those of 3D-like counterpart, manifesting energetic barriers between the underlying charge transport layer and 3D-like HP photoactive layer. Such energetic landscape, in turn, can impede efficient charge transport across the vertical direction, and consequently, curtail PV performances. Indeed, those quasi-2D HP films exhibit low PV performances (**Figure S12**, detailed device fabrication and characterizations in Experimental Section); here, an optimal 3D composition ratio of 60%, where the exclusive emergence of 3D-like phases is expected to be most probable, was employed. These observations suggest that mitigation of vertical phase inhomogeneities in the quasi-2D HPs is vital for demonstrating efficient PV devices.

Note that NMF analysis also identifies similar phase emergence behaviors at both

the top and bottom surface of the BDA-based quasi-2D HPs (**Figure 2b, S10b and S11**), again revealing the vertically homogenized phase distributions in this system. While this feature can benefit the optoelectronic performances when the films are employed in PV devices, however, an extremely low power conversion efficiency (PCE) of 0.39% is recorded (**Figure S12**). Such a poor PV performance is likely attributed to considerable charge carrier loss through the abundant surface defects as well as the emergence of non-HP δ-$CsPbI_3$ crystallites in the quasi-2D HP matrices (*vide infra*).

Local Phase Inhomogeneities and Chemical Interactions in the Quasi-2D HPs

Exploration of the global phase emergence behaviors in the quasi-2D HP systems reveal that various HP crystallites emerge, thus causing notable phase inhomogeneities in the film matrices. To spatially resolve and investigate the local phase inhomogeneities in the synthesized film matrices, Hyperspectral cathodoluminescence (CL) microscopy, integrated with a Scanning electron microscope (SEM), is utilized. **Figure 3a** shows the surface SEM images of the quasi-2D HP films with different spacer cations. Here, a fixed 3D ratio of 60% was adopted for constructing quasi-2D HP films, which most likely offer 3D-like matrices as deduced from NMF analysis. It was found that the selection of a molecular spacer renders a distinctive surface morphology.

The BA-based film exhibits a rough and crumbled surface morphology with many voids (diameters of 100-300 nm), suggesting that considerable defects are likely present in the matrix. Particularly, the voids can be attributed to the low boiling point of BA (78 ^{o}C), which can facilitate its vaporization upon film fabrication. In the BDA-based film, rod-shaped structures emerge. It is found that these features are exactly overlapped with the emission signals in the corresponding 445 nm-filtered CL map, which is confirmed as δ-$CsPbI_3$ (**Figure 3b**)[41, 42]. Note that appreciable 445-nm signals are also observed in BA-based quasi-2D HP film, although the corresponding crystallites are not found in the SEM image. This suggests that the δ-$CsPbI_3$ crystallites are intercalated within the HP matrices, as a result of the deformation from the 3D-like phases[41-43]. In contrast, the rod-shaped δ-$CsPbI_3$ crystallites at the BDA-HP film surface corroborate that both HP and non-HP phases are concurrently constructed upon the crystallization process, rather than deformation[42, 43]. We hypothesize that, the slow crystallization dynamics in this system, attributed to the strong chemical interaction between BDA and inorganic precursors, causes the separated growth of the quasi-2D HPs and non-HP phases, rather than promoting the higher-*n* HP growths (*vide infra*).

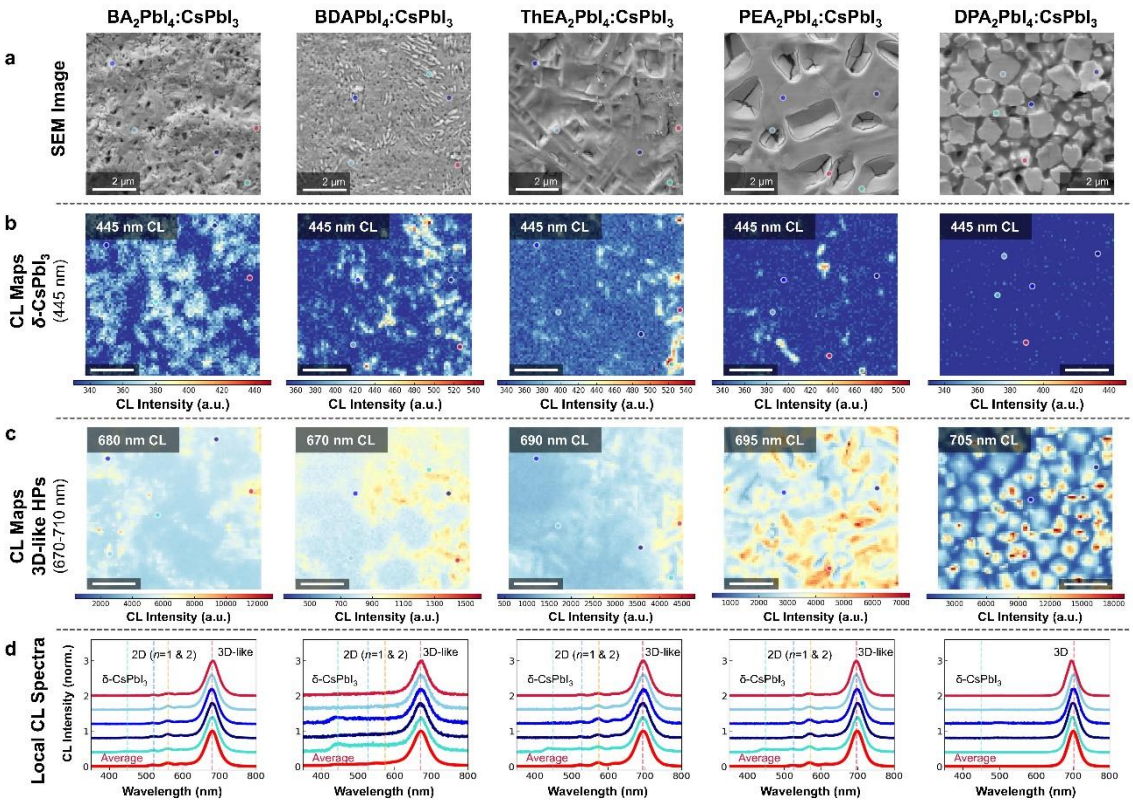

Figure 3. Hyperspectral cathodoluminescence (CL) microscopy characterizations. (a) SEM images and the corresponding (b) 445- and (c) 670-710 nm-filtered CL intensity maps of the quasi-2D HP films with different spacer cations. (d) Local CL spectra collected at the 5 different spots (marked with colored circles in the SEM images and the CL maps) in each film. For each case, an average CL spectrum (across the scanned area) is also included (red curve).

Also, a large number of voids (smaller than the BA counterpart; <100 nm) are observed. Given the high boiling point of BDA (~158 ºC), those voids can be attributed to the both slower crystallization kinetics of DJ-type 2D HPs and thermodynamic preference of the δ-$CsPbI_3$ formation at the low processing temperature[44, 45]. We map the CL signals at ~680-700 nm for each film (**Figure 3c**). These wavelengths respectively correspond to the CL peak of the 3D-like HPs (the average and local CL spectra collected from each film are shown in **Figure 3d**). In both cases, stronger CL signals of 3D-like phases are observed in the surface voids. Similar CL intensity enhancements were observed from the grain boundaries in 3D HP films, attributed to the higher free carrier concentrations promoting radiative recombination[42, 46]. Given such voids are associated with the evaporation of the spacer, it is hypothesized that large amounts of molecular spacers are congregated at the local sites. In turn, this can manifest a higher density of the coordinated spacers on the HP surface, thereby passivating the surface defects and accelerating radiative recombination[47].

ThEA- and PEA-based quasi-2D HPs exhibit softer surface morphologies than BA and BDA counterparts. ThEA-based film exhibits angulated surface textures, likely

attributed to the formation of small-*n* 2D HP phases. Also, rectangular particles exhibiting 445 nm CL are intercalated to the film surface (**Figure 3a** and **3b**), indicating that δ-$CsPbI_3$ also emerges in this system. Note that the area exhibiting the local δ-$CsPbI_3$ signals is smaller than that in the BA-based system. These suggest that ThEA offers better stability of the 3D-like phases than BA, though it is still insufficient to realize PV-grade films. The PEA-based film renders a flat and smooth surface morphology, though some of the areas exhibit collapsed features. Note that the local spots emitting δ-$CsPbI_3$ are notably reduced and there was no appreciable structural feature correlating with the emission spots (**Figure 3c**). This indicates that PEA offers much more improved phase stability of quasi-2D HPs than ThEA, thereby suppressing phase deformation. Meanwhile, stronger CL intensities of 3D-like HPs are observed along the cracked boundaries in the films. Such a distinct local contrast in 3D-like HP CL indicates that substantial chemical inhomogeneities are manifested in the film surface, which can disturb the energetic landscape and thereby hamper efficient charge transport.

Flat and island-like features are distinctively observed in the DPA-based quasi-2D HP films (**Figure 3a**). Interestingly, no appreciable CL signal associated with δ-$CsPbI_3$ is observed (**Figure 3b**), attributed to the outstanding phase stabilizing effect of DPA. The 3D-like HP phases exhibit CL peaked at the longer wavelength of 705 nm (**Figure 3c**) than that of the others, which almost replicates the emission of bulk $CsPbI_3$[40]. This indicates DPA manifests the formation of thicker 3D-like HPs at the top surface. The steric hindrance between the neighboring DPA phenyl rings can restrict the complete surface coverage of the spacers on the HP lattice. This scenario can impede the termination of crystallization as 2D HP phases, thereby promoting the formation of thicker HP lattices. Note that some immature crystallites, without offering flat and island-like structures, are observed. Local CL spectra reveal that these structures exhibit blueshifted CL (~10nm) peaks (Crimson-colored curve, **Figure 3d**), indicating the formation of quasi-2D HPs thinner than those at the foremost top surface. This suggests that DPA cations are more abundant along the depth of the film, which can make more dimension-confined HP lattices.

Overall, among these molecular spacers, it is anticipated that PEA-based quasi-2D film is the most suitable photoactive matrix. Despite notable chemical inhomogeneity, it can offer a stable and smooth film surface while minimizing the local phase inhomogeneity, which benefit PV performances and stability. In contrast, such an imperfect surface coverage of the crystallites in the DPA-based quasi-2D HP film is not expected to offer good charge transport features and PV performances, though the DPA indeed bestows excellent stability of the photoactive 3D-like phases.

To gain insights into the crystallographic information, we collected grazing-incidence wide-angle X-ray scattering (GIWAXS) patterns of the quasi-2D HP films (**Figure S13a-c**). We apply three different incidence angles, 0.1, 0.2 and 0.5°, where the small and large angles majorly reflect the crystallographic information of the foremost surface and the bulk interior of the films, respectively. This allows us to explore the progressive change in phase emergence behaviors along the vertical directions.

The BA-based film exhibits strong Bragg spots aligned along the Q_z=~1.0 and ~2.0 Å^{-1}. This is a representative signature for the vertically aligned 3D HP lattice, which has been observed from various quasi-2D HP systems[14]. That is, BA promotes the growth of vertically aligned 3D-like HP phases. **Figure S14a** shows the corresponding 1D scattering profiles of the BA-based quasi-2D HP film along the out-of-plane (OOP) and in-plane (IP) directions, respectively. In addition to the 3D $CsPbI_3$ lattice, scattering modes of *n*=1 and 2 2D HPs are observed. These peaks become stronger with increasing the angle of the X-ray beam, particularly along the OOP direction, indicating that these face-on stacked 2D HP phases become dominant towards the bottom surface. Meanwhile, appreciable peaks of δ-$CsPbI_3$ and PbI_2 are observed. These phases are produced as a result of the deformation of quasi-2D HP[41-43], indicating its poor stability in agreement with the emission behavior.

Distinctive Debye-Scherrer rings are observed in the 2D GIWAXS pattern of the BDA-based film, suggesting the crystallites in the matrix majorly exhibit random orientation (**Figure S14b**). In the corresponding 1D profiles, strong scattering peaks of δ-$CsPbI_3$ and PbI_2 crystallites are observed, indicating the predominance of these phases. Note that these peaks are relatively stronger than the 3D $CsPbI_3$ peak at the lower incidence angles, suggesting these degradation products are located around the top of the film surface.

The 2D GIWAXS patterns of the ThEA-based film majorly exhibit ring-shaped patterns, whereas the peaks of the principal 2D HPs (e.g., *n*=1 and 2 phases) are strong along the OOP direction (**Figure S14c**). These 2D HPs become predominant at the bottom, which agrees well with the vertical phase inhomogeneity seen in PL observations. Meanwhile, the emergence of weak Braggs spots along the Q_z=~1.0 Å^{-1} indicates that the 3D-like HP phases in this system are also vertically aligned. Moreover, strong emergences of δ-$CsPbI_3$ and PbI_2 crystallites corroborate that ThEA cannot bestow good phase stability of the resulting quasi-2D HPs. In the PEA-based film, the Braggs spots become more discrete, whereas the scattering rings are weakened (**Figure S14d**), suggesting more oriented growth of the crystallites in the matrix. According to the 1D scattering patterns, overall, similar phase emergence and vertical phase inhomogeneities are observed in the PEA-based system. A stark difference from ThEA counterpart is the absence of the δ-$CsPbI_3$ and PbI_2 crystallites. This further corroborates that PEA indeed offers good stability in the quasi-2D HP thin films.

The DPA-based HPs exhibit random-oriented crystallographic features, as confirmed by the ring-shaped scattering patterns (**Figure S14e**). Similar to the PEA-based system, there was no appreciable signal from the δ-$CsPbI_3$ and PbI_2 crystallites in the DPA-based quasi-2D HPs. Although this indicates that DPA can provide stable 3D-like HP lattices, such random-oriented crystallites, together with the distinctive abundance of *n*=1 and 2 2D HPs, infer inefficient charge transport environments that are likely detrimental to PV applications.

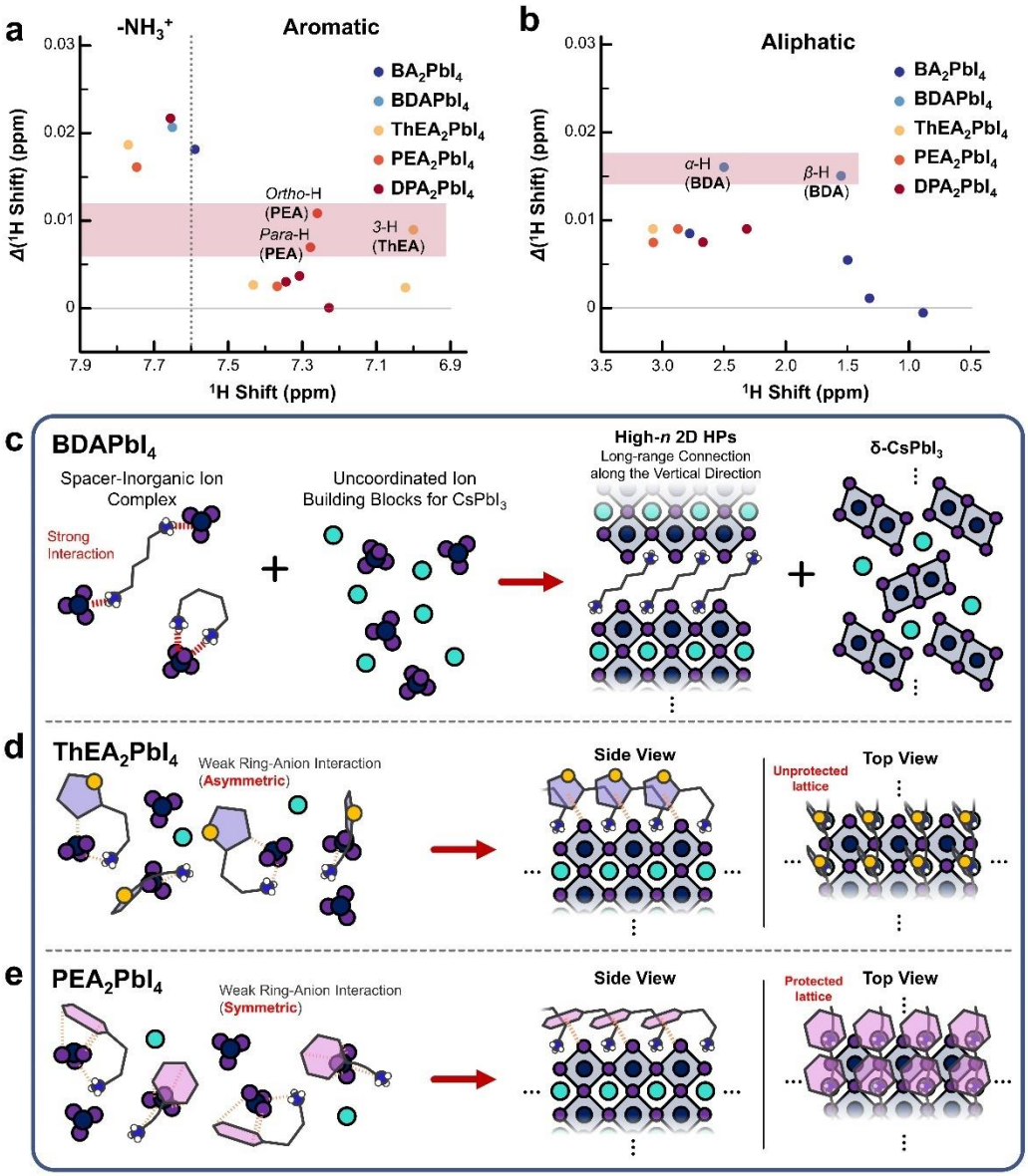

Figure 4. Estimated magnitudes of proton downshifts, Δ(^{1}H Shift), of the protons in the (a) ammonium and aromatic group, and (b) alkyl chains for the corresponding spacer cations in the precursor solutions, derived from the solution-phase ^{1}H nuclear magnetic resonance (NMR) spectra. Schematics describing the chemical interaction and the molecular geometry between the spacer cation and the inorganic building blocks for (c) BDA, (d) ThEA, and (e) PEA-based quasi-2D HP systems, respectively.

To gain an understanding of the chemical interaction between the molecular spacers and precursors, which can affect the crystallographic structures and phase distributions in the films, proton nuclear magnetic resonance (^{1}H-NMR) spectroscopy is conducted on the corresponding precursor solutions. **Figure S15 and S16** exhibit ^{1}H-NMR spectra of the precursor solutions, together with the corresponding solution after dissolving spacer cation-iodide salts, allowing us to identify the chemical changes by the interaction with the inorganic ions.

For all cases, the -NH_3^+ peak undergoes notable downfield shifts (~0.02 ppm) when the inorganic precursors are incorporated, indicating the strong chemical interaction between the ammonium group and the inorganic precursors (**Figure 4a**). In addition, for BA, the characteristic peaks of hydrogens at *α*-carbons also exhibit appreciable downfield shifts in the precursor solution (**Figure S15a and Figure 4b**), indicating that partial electron transfer from BA to the inorganic precursors occurs. Note that the progressive weakening of the ^{1}H downfield shifts is observed from *β*- to δ-protons position where the latter does not exhibit appreciable peak shift. This suggests that the electrostatic interaction mainly takes place in the ammonium group. In BDA, the protons at both the *α*- and *β*-carbon exhibit strong and comparable downfield shifts (~0.016 ppm) when the inorganic precursors are present (**Figure S15b and Figure 4b**). This indicates the existence of a strong chemical interaction between the inorganic ions and the BDA molecules – across the entire molecular structure. Presumably, two interactive sites (i.e., ammonium groups) in BDA manifest tight coordination with the HP building blocks in the solution phase (**Figure 4c**). Such strong chemical interaction between spacer and inorganic building blocks not only offers slow crystallization kinetics but also maintaining the ionic coordination during the entire film fabrication process – starting from liquid-air (top) to the liquid-substrate (bottom) interfaces. This likely mitigates the vertical phase inhomogeneity of the quasi-2D HP matrix. However, as the spacer-precursor interaction is too strong, some of the 3D $CsPbI_3$ precursors cannot be involved for the crystallization of quasi-2D HP lattice. Subsequently, a separate crystallization of these 3D precursors take place, which are likely form δ-$CsPbI_3$ that are intercalated into the film matrix, due to the thermodynamic incompatibility of the α-HP phase at such a low annealing temperature.

In both ThEA and PEA, the protons at -NH_3^+ and the alkyl bridge exhibit sequential downfield shifts as seen in the BA system (**Figure S15c and S15d**), suggesting the spacers primarily interact with the inorganic ions through the ammonium head. In contrast, only the proton at the 3-carbon in ThEA (marked with a yellow circle) exhibits appreciable downfield shifts (**Figure S16a**), whereas the protons at ortho- and para-positions of PEA undergo such downfield shifts (**Figure S16b and Figure 4a**). This suggests that the respective chemical interaction between the spacer and precursor ions manifests different molecular geometry of ThEA and PEA in the solutions. Specifically, ThEA renders an asymmetric molecular geometry, where both the ammonium head and 3-carbon in the thiophene ring interact with the inorganic ions (**Figure 4d**). In contrast, PEA can offer symmetric molecular geometry that the phenyl ring faces on the inorganic ions (**Figure 4d**). We hypothesize that such molecular geometry can be maintained even during the crystallization process. This in turn manifests the distinctive ring alignments at the HP surfaces for each case, thus bestowing a stark difference in phase stability upon ambient exposures. The upright geometry of ThEA cannot protect the HP lattice and compromise the lattice stability (**Figure 4d**). In contrast, PEA's 'umbrella' geometry can effectively block the environmental O_2 and H_2O, thus effectively protecting the inorganic lattice and improving the phase stability (**Figure 4e**) – consistent with the conclusion based on PL, CL and GIWAXS observations. Similar symmetric molecular geometry is anticipated from the ^{1}H NMR spectra of the DPA-based system (**Figure S15e and**

S16c), which strongly agrees with our observations.

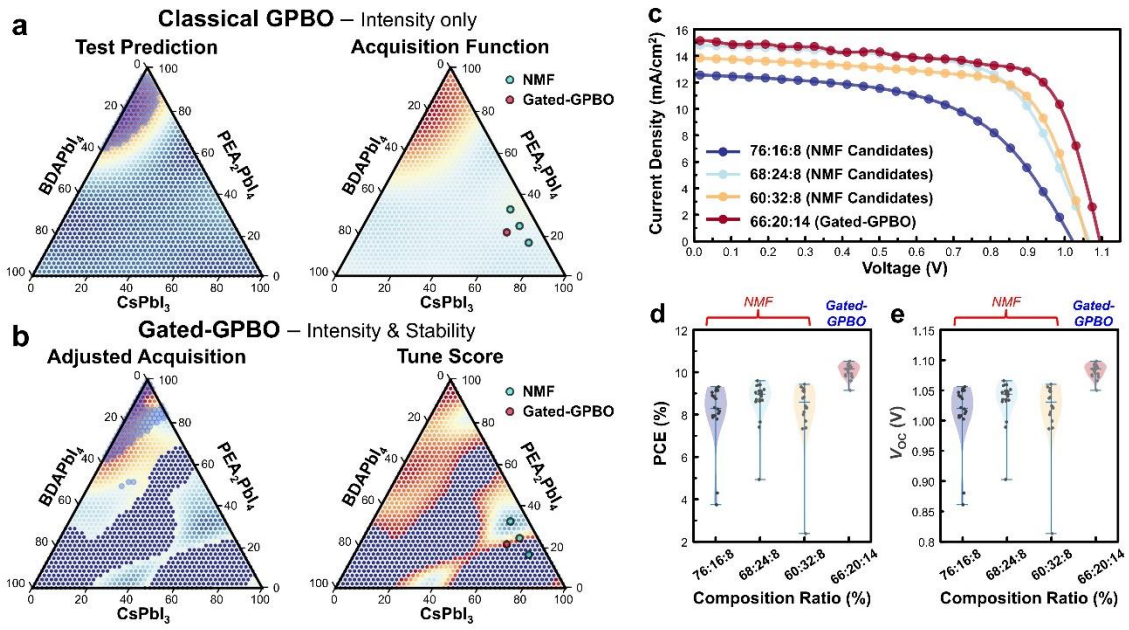

Figure 5. Ternary-compositional maps of target functionality of the quasi-2D HPs visualized by (a) classical BO and (b) Gated-GPBO, respectively. (c) *J-V* curves of the champion PVs employing quasi-2D HPs photoactive layer designed by NMF and Gated-GPBO. (d,e) Statistical plots of (d) PCE and (e) V_{OC} of PV devices employing quasi-2D HPs photoactive layer designed by NMF and Gated-GPBO (based on 20 individual devices).

Machine Learning-Driven Exploration of Ternary Quasi-2D HP system

The high-throughput exploration and detailed chemical and structural analysis reveal the profound roles of spacer cations in making quasi-2D HPs. Among them, BDA homogenizes the vertical phase distribution while compromising phase stability, whereas PEA offers a flattened HP surface with excellent phase stability at the expense of vertical phase inhomogeneity. Considering these features, it is reasonable that employing both spacer cations to quasi-2D HPs can synergistically allow us to exploit the advantages of each component while compensating for the drawbacks.

Inspired by this hypothesis, we designed a ternary compositional space by using $BDAPbI_4$, PEA_2PbI_4, and $CsPbI_3$ as endmembers, and the phase emergence behaviors of this new combinatorial library are explored via high-throughput automated experimental workflow. **Figure S17a** exhibits the synthesized quasi-2D HP arrays where the exact composition ratios in each film are summarized in **Figure S17b**[26]. Similar to the binary systems, time-evolved PL spectra of the films are collected at the top and bottom surfaces, as shown in **Figure S18**.

To effectively identify the global phase emergence behaviors, we employ NMF deconvolution to the PL datasets with four optimal components (**Figure S19**). Here we

implemented Gaussian processing (GP) regression to compensate for the uncertainty caused by the large compositional steps (8%), which effectively interpolates between the NMF components in the loading maps[26]. In both top and bottom surfaces, the emergence maps of n=1, n=2-3, n≥4 2D, and 3D-like HP phases in the ternary compositional space are visualized. We focus on the phase emergence behaviors of the 3D-like HPs (i.e., Phase Set 4 in Figure 5a), which shows high probabilities at the lower right corner in the ternary phase diagram – <15% $BDAPbI_4$, 15-40% PEA_2PbI_4, and 60-70% $CsPbI_3$ – for both the top and bottom surfaces. That is, the compositions within this range are anticipated to provide 3D-like HP phases while the vertical phase inhomogeneities are greatly mitigated. Specifically, we manually select three compositions – $CsPbI_3$:PEA_2PbI_4:$BDAPbI_4$ of 76:16:8, 68:24:8, and 60:32:8 – as optimal coordinates in the ternary diagram, which is likely suitable for PV applications. Indeed, the ternary quasi-2D HPs film with a 60:32:8 composition ratio exhibits a homogenized, and δ-$CsPbI_3$-free surface, as seen in hyperspectral CL characterization (**Figure S20**), validating the effectiveness of NMF-based prediction.

To further explore the ternary compositional space and thereby realize the optimized 3D-like HP matrix for the PV applications, we employ a newly developed Gated-GPBO approach to drive the exploration within the compositional space. We first implement a classical GPBO which solely takes account into the PL intensity of the films (**Figure 5a**). In the Gated-GPBO, an additional GP model that takes accounts into an instability score to find the compositions that render a stable PL peak that is close to the target wavelength (>600 nm). Details regarding the Gated-GPBO approach can be found in Methods. The Gated-GPBO predicted ternary diagrams manifesting the target functionalities are shown in **Figure 5b**. It is found that the target functionality intensely emerges close to the compositional space where NMF is predicted (Phase Set 4 in Figure 4a). Specifically, it visualizes a narrow channel along the ~50% $CsPbI_3$ line profile. We refine a ternary composition 66:20:14 as a Gated-GPBO-designed composition, which is collectively shown with the NMF-predicted compositions in Figure 5b.

To comparatively validate the functionality of quasi-2D HPs with designed compositions that NMF-based prediction and Gated-GPBO respectively suggested, we assess the performances of p-i-n type PVs employing these matrices as a photoactive layer; a device architecture of ITO / poly[bis(4-phenyl)(2,4,6-trimethylphenyl)amine] (PTAA) / Poly(9,9-bis(3'-(*N*,*N*-dimethyl)-*N*-ethylammoinium-propyl-2,7-fluorene)-alt-2,7-(9,9-dioctylfluorene))dibromide (PFN-Br) / quasi-2D HP / C_{60} / Bathocuproine (BCP) / Ag is used. **Figure 5c** shows the current-voltage curves of the champion PVs employing the corresponding quasi-2D HP films. Without any optimizations, the quasi-2D HP film designed by Gated-GPBO demonstrates the highest PV performance with a PCE of 11.16%, showing ~15-60% enhancements compared to the performances of PV with NMF-predicted films (Detailed PV parameters are summarized in **Table S1**). Such a higher PCE of the Gated-GPBO-designed PV is majorly gained by the improvements in open-circuit voltage (V_{OC}) and fill factor (FF). This indicates that the carrier loss is greatly suppressed in the Gated-GPBO-designed film, likely attributed to better chemical homogenization of the quasi-

2D HP lattice. It should be noted that the films are synthesized at a low annealing temperature (95 ^{o}C), without any dedicated efforts in additional chemical and device engineering. This indicates that the Gated-GPBO-designed quasi-2D HP still has potential realizing high performances, on par with those of widely used large-bandgap sub-cells that are required for tandem applications[48].

Figure 5d, 5e and **Figure S21** exhibits statistical distributions of PV parameters (PCE, V_{OC}, and J_{SC} and FF, respectively) for each PV configuration – estimated from 20 individual devices, obviously showing that the PV performances are reproducible. These results also validate the effectiveness of the Gated-GPBO for materials design used in this study, which can significantly accelerate the discovery of new functional materials realizing high PV performances from massive complex materials space.

Outlook

In summary, we systematically explore the chemical space of the Cs-based quasi-2D HPs – defined by the spacer cations – that determines their phase complexity by implementing high-throughput automated experimental workflow. Through high-throughput PL spectroscopy and ML-based data analysis, several key features are observed. The RP-type molecular spacers with high molecular weights exhibit slow crystallization dynamics, thus manifesting the growth of 3D-like HP phases – more stable than the pure 3D $CsPbI_3$ counterpart. DJ-type spacer exhibit stronger chemical interactions between the spacers and inorganic building blocks, which is maintained during the overall crystallization sequence – starting from top to bottom. The resulting quasi-2D HP matrices exhibit mitigated vertical phase inhomogeneities, although the films exhibit poor stability and the non-HP δ-$CsPbI_3$ crystallites are involved. It is found that the molecular geometry of spacer plays a crucial role in realizing the stable quasi-2D HP lattices. The spacers with homocyclic, phenyl groups (PEA and DPA) exhibit a geometrically symmetric spacer-precursor interaction, which renders stable 3D-like HPs effectively protected by the aromatic rings. In contrast, the spacer with heterocyclic ring (ThEA) manifests asymmetric chemical interaction in the precursor state. This renders an upright molecular geometry at the 3D-like HP surface that cannot protect the lattice against O_2 or H_2O, thereby resulting in poor phase stability. These observations reveal the distinctive working principles of the spacer cations in the corresponding crystallization mechanisms, which have not been systematically identified so far. Thus, our findings provide new insights into the selection principles of molecular spacer for designing quasi-2D HPs.

To exploit the beneficial effects of molecular spacers – homogenizing vertical phase distribution and achieving high phase stability, the BDA and PEA-based ternary-composition quasi-2D HP system is explored. Here, we develop and deploy an active learning algorithm, a Gated-GPBO-based compositional exploration workflow. This allows for iterative discovery of specific compositions realizing target functionalities from a discrete chemical space of the molecular spacers in quasi-2D HPs, where the classical BO cannot achieve it. The quasi-2D HP film, with compositionally tailored by the Gated-GPBO indeed demonstrates the suited bandgaps and high PV

performances, exhibiting promising functionalities and manufacturability for tandem PV applications. This work presents an effective experimental data-driven experimental workflow, which realizes bespoke design of optoelectronic functionalities and thus, substantially accelerates materials discovery for sustainable applications.

Acknowledgements

M.U., S.L.S., H.S. contributed equally to the work. M.A. acknowledge support from National Science Foundation (NSF), Award Number No. 2043205 and Alfred P. Sloan Foundation (Award No. FG-2022-18275). M.U. and J.Y. acknowledge support from Yonsei University Research Fund of 2024-22-0106. The hyperspectral CL microscopy and Gated-GPBO development were supported by the Center for Nanophase Materials Sciences (CNMS), which is a US Department of Energy, Office of Science User Facility at Oak Ridge National Laboratory. This research was also supported by BrainLink program (NRF-2022H1D3A3A01077343) and Nano·Material Technology Development Program (NRF-2021M3H4A1A02049634) through the National Research Foundation of Korea (NRF) funded by Ministry of Science and ICT. H.S. acknowledge support from the Basic Science Research Program through the National Research Foundation of Korea (NRF), funded by the Ministry of Education (RS-2023-00276169).

Experimental Section

High-throughput automated synthesis and optical characterization

Stoichiometric 2D A_2PbI_4 (A=BA,ThEA, PEA, and DPA) or A'PbI_4 (A'=BDA), and 3D $CsPbI_3$ precursor endmembers in DMF:DMSO solution (9:1, 0.4 M) were prepared by dissolving the materials in an N_2 glove box. These solutions were stirred overnight at room temperature, and then transferred to a pipetting robot system (Opentrons, OT-2) in the N_2-purged box.

We implemented an experimental workflow for high-throughput robotic synthesis, according to our previous reports[13, 14, 26-29]. By using a 300 μL-capacity single-channel pipet, 2D and 3D endmember solutions are combinatorially mixed to achieve 50 μL of quasi-2D binary or ternary precursor mixtures with the designed compositional ratio for each well. Separately, the glass substrates, after sequential washing with acetone and isopropyl alcohol, are exposed to UV/O_3-treatment for 20 min. Then, the substrates are quickly transferred to the chamber for the pipetting robot system. For film fabrication, 0.5 μL of the prepared solutions were drop-casted onto the UV/O_3-treated glass substrates, which were already heated to 95 °C by using a heating module. The droplets of quasi-2D HP precursors are then crystallized at 95 °C for 10 min.

The synthesized quasi-2D HP film arrays were quickly mounted to a multi-mode optical reader (BioTek, Cytation 5) and time-evolved PL spectra of each film (1 nm step size) were collected alternatively at the top and bottom of the film surface, using 365 nm

excitation beam. The emission spectra from each film spot were obtained as one ‘read cycle’ every 15 mins for 96 films. The read cycle was repeated for 10 hours. A PL read sequence is designed for the alternating scan of both the top and bottom surface, obtaining the time-evolved PL spectra from both the top and bottom over time. This results in the actual time interval between the read cycles at each position being 30 min. In Gen5 software, we adjusted the spot size of the excitation beam to be <3 mm in diameter, allowing for confining the excited area in each film. This not only suppresses the emission crosstalk caused from the neighboring films but also excludes undesired characterization of the edge of the film that can have different phase constitutions.

NMF deconvolutions for PL datasets

NMF data analysis was performed on google Colab using Python 3.6 and scikit-learn 0.22.1 library. The codes are available in the following link (Google Colab):

https://drive.google.com/file/d/1HzfvqLHVUY-WvPvLCO1Vrpxt2bVUE6wC/view?usp=drive_link

https://drive.google.com/file/d/1YgGM5jA9OcQP0Ic64HjIYPYbYOHqmyGB/view?usp=drive_link

https://drive.google.com/file/d/1Eg_uzc5PYnkOPfP0iQSsKfSiHVloBNgV/view?usp=drive_link

https://drive.google.com/file/d/1sTuCKfkoPqn3l-O_srCbQQ_mc9RZLhyY/view?usp=drive_link

https://drive.google.com/file/d/1rn-RZCq9ra4uzP3CK5fnhxptBYEGwOMy/view?usp=drive_link

https://drive.google.com/file/d/1t3b9HmpTyXYdY73LzwjngmXAyl5DQmRK/view?usp=drive_link

Gated Gaussian Process (GP) Bayesian Optimization (BO)

Gated-GPBO approach leverages two GP models to optimize experimental exploration by dynamically refining the search space based on complementary insights. In this work, the primary GPBO is tasked with maximizing PL intensity; an additional Gate-GP operates in tandem with the primary GP, focusing on actively refining the compositional space by evaluating the "instability score" derived from the temporal evolution of PL spectra. As the Gate-GP identifies compositions with higher instability scores, it provides feedback to the primary GP, guiding it away from these compositions and towards compositional space where likely leads to both high PL intensity and good stability. The notebook of the Gated-GPBO-driven exploration is publicly available at https://github.com/SLKS99/Automated-Discovery-and-Optimization-of-Molecular-Spacers-in-Cs--Based-Quasi-2D-Perovskites, allowing readers to adapt and deploy gated-GPBO in various experiments.

Materials characterizations

Hyperspectral CL microscopy was conducted by using an environmental SEM instrument (FEI, Quattro) with a Delmic Sparc CL collection module. A parabolic mirror was utilized to collect the CL signals upon e-beam excitation. An e-beam with an acceleration voltage of 5 kV (beam current of 28 pA), with an acquisition time of 100 ms was used. A square pixel with a size of 100 × 100 nm^2 was used. All measurements were conducted in a low vacuum environment of 0.02 Torr with H_2O vapor, which effectively alleviated sample charging while minimizing e-beam-induced damage.

2D GIWAXS measurements were carried out at the 9A beamline (U-SAXS) at the Pohang Accelerator Laboratory in Pohang, Republic of Korea. The beam energy used was 11.07 KeV. Three different incidence angles, 0.1°, 0.2°, and 0.5° were used to explore the depth-dependent crystallographic properties of the quasi-2D HP films.

Solution phase ^1H NMR spectra were collected by a 400 MHz NMR spectrometer (Bruker, Avance III HD), with DMSO-d_6 as a solvent.

Solar cell fabrication and characterization

For PV device fabrication, ITO substrates were cleaned in deionized water (DI water), acetone, and 2-propanol by ultrasonic treatment for 10 min each. After drying the substrates in an oven, the ITO substrates were treated with UV/O_3 for 20 min and then transferred to a N_2 glovebox. Subsequently, PTAA (1.5 mg/ml in Tol) was spin-coated on ITO at 3000 rpm for 30 s and annealed at 100 °C for 10 min. The perovskite precursor with a concentration of 1.0 M was prepared by mixing CsI, AI (A=BA, ThEA, PEA, and DPA), $BDAI_2$ and PbI_2 according to the composition ratio of $CsPbI_3$, A_2PbI_4, $BDAPbI_4$ in a mixed solution of DMF and DMSO (3:1 v/v). Before the perovskite spin-coating, the substrates were pre-heated at 60 °C for better wettability and crystallization. The perovskite precursor was spin-coated at 2000 rpm for 20 s and annealed at 100 °C for 10 min. After cooling down to room temperature, the substrate was transferred to a vacuum chamber and C_{60} (30 nm), BCP (7 nm) and Ag (100 nm) were sequentially deposited on the perovskite film under a pressure of ~10^{-6} torr.

The *J-V* curves of the PV devices were measured in a N_2 glove box using a solar simulator (Newport-Oriel 94083A, Class AAA) synchronized with a Keithley source meter 2400. The light intensity was calibrated to 100 mW/cm^2 using an NREL-certified Si-reference cell. To restrict the active cell area to 0.0314 cm^2, the PSCs of a specific size were masked using a shadow metal mask.

References

1. Lim, J.; Park, N. G.; Seok, S. I.; Saliba, M., All-perovskite tandem solar cells: from fundamentals to technological progress. *Energ Environ Sci* **2024,** *17* (13), 4390-4425.

2. Lin, R. X.; Wang, Y. R.; Lu, Q. W.; Tang, B. B.; Li, J. Y.; Gao, H.; Gao, Y.; Li, H. J.; Ding, C. Z.; Wen, J.; Wu, P.; Liu, C. S. Y.; Zhao, S. Y.; Xiao, K.; Liu, Z.; Ma, C. Q.; Deng, Y.; Li, L. D.; Fan, F. J.; Tan, H. R., All-perovskite tandem solar cells with 3D/3D bilayer perovskite heterojunction. *Nature* **2023**.

3. Lin, R. X.; Xu, J.; Wei, M. Y.; Wang, Y. R.; Qin, Z. Y.; Liu, Z.; Wu, J. L.; Xiao, K.; Chen, B.; Park, S. M.; Chen, G.; Atapattu, H. R.; Graham, K. R.; Xu, J.; Zhu, J.; Li, L. D.; Zhang, C. F.; Sargent, E. H.; Tan, H. R., All-perovskite tandem solar cells with improved grain surface passivation. *Nature* **2022,** *603* (7899), 73-+.

4. Song, H.; Yang, J.; Lim, S. G.; Lee, J.; Jeong, W. H.; Choi, H.; Lee, J. H.; Kim, H. Y.; Lee, B. R.; Choi, H., On the surface passivating principle of functional thiol towards efficient and stable perovskite nanocrystal solar cells. *Chem Eng J* **2023,** *454*.

5. Hassan, Y.; Park, J. H.; Crawford, M. L.; Sadhanala, A.; Lee, J.; Sadighian, J. C.; Mosconi, E.; Shivanna, R.; Radicchi, E.; Jeong, M.; Yang, C.; Choi, H.; Park, S. H.; Song, M. H.; De Angelis, F.; Wong, C. Y.; Friend, R. H.; Lee, B. R.; Snaith, H. J., Ligand-engineered bandgap stability in mixed-halide perovskite LEDs. *Nature* **2021,** *591* (7848), 72-+.

6. Li, S.; Zheng, Z.; Ju, J. Q.; Cheng, S. Y.; Chen, F. Y.; Xue, Z. X.; Ma, L.; Wang, Z. P., A Generic Strategy to Stabilize Wide Bandgap Perovskites for Efficient Tandem Solar Cells. *Adv Mater* **2024,** *36* (9).

7. Steele, J. A.; Jin, H. D.; Dovgaliuk, I.; Berger, R. F.; Braeckevelt, T.; Yuan, H. F.; Martin, C.; Solano, E.; Lejaeghere, K.; Rogge, S. M. J.; Notebaert, C.; Vandezande, W.; Janssen, K. P. F.; Goderis, B.; Debroye, E.; Wang, Y. K.; Dong, Y. T.; Ma, D. X.; Saidaminov, M.; Tan, H. R.; Lu, Z. H.; Dyadkin, V.; Chernyshov, D.; Van Speybroeck, V.; Sargent, E. H.; Hofkens, J.; Roeffaers, M. B. J., Thermal unequilibrium of strained black $CsPbI_3$ thin films. *Science* **2019,** *365* (6454), 679-+.

8. Swarnkar, A.; Marshall, A. R.; Sanehira, E. M.; Chernomordik, B. D.; Moore, D. T.; Christians, J. A.; Chakrabarti, T.; Luther, J. M., Quantum dot-induced phase stabilization of α-$CsPbI_3$ perovskite for high-efficiency photovoltaics. *Science* **2016,** *354* (6308), 92-95.

9. Li, X. T.; Hoffman, J. M.; Kanatzidis, M. G., The 2D Halide Perovskite Rulebook: How the Spacer Influences Everything from the Structure to Optoelectronic Device Efficiency. *Chem Rev* **2021,** *121* (4), 2230-2291.

10. Soe, C. M. M.; Nagabhushana, G. P.; Shivaramaiah, R.; Tsai, H. H.; Nie, W. Y.; Blancon, J. C.; Melkonyan, F.; Cao, D. H.; Traoré, B.; Pedesseau, L.; Kepenekian, M.; Katan, C.; Even, J.; Marks, T. J.; Navrotsky, A.; Mohite, A. D.; Stoumpos, C. C.; Kanatzidis, M. G., Structural and thermodynamic limits of layer thickness in 2D halide perovskites. *P Natl Acad Sci USA* **2019,** *116* (1), 58-66.

11. Quan, L. N.; Yuan, M. J.; Comin, R.; Voznyy, O.; Beauregard, E. M.; Hoogland, S.; Buin, A.; Kirmani, A. R.; Zhao, K.; Amassian, A.; Kim, D. H.; Sargent, E. H., Ligand-Stabilized Reduced-Dimensionality Perovskites. *J Am Chem Soc* **2016,** *138* (8), 2649-2655.

12. Lee, J. W.; Dai, Z. H.; Han, T. H.; Choi, C.; Chang, S. Y.; Lee, S. J.; De Marco, N.;

Zhao, H. X.; Sun, P. Y.; Huang, Y.; Yang, Y., 2D perovskite stabilized phase-pure formamidinium perovskite solar cells. *Nat Commun* **2018,** *9*, 3021.

13. Yang, J.; Lawrie, B. J.; Kalinin, S. V.; Ahmadi, M., High-Throughput Automated Exploration of Phase Growth Behaviors in Quasi-2D Formamidinium Metal Halide Perovskites. *Advanced Energy Materials* **2023,** *13* (43), 2302337.

14. Yang, J. H.; Hidalgo, J.; Song, D. H.; Kalinin, S. V.; Correa-Baena, J. P.; Ahmadi, M., Accelerating Materials Discovery by High-Throughput GIWAXS Characterization of Quasi-2D Formamidinium Metal Halide Perovskites. *Adv Funct Mater* **2024**.

15. Jeon, N. J.; Noh, J. H.; Kim, Y. C.; Yang, W. S.; Ryu, S.; Seok, S. I., Solvent engineering for high-performance inorganic-organic hybrid perovskite solar cells. *Nat Mater* **2014,** *13* (9), 897-903.

16. Song, H.; Kim, H. B.; Cho, S. C.; Lee, J.; Yang, J.; Jeong, W. H.; Won, J. Y.; Jeong, H. I.; Yeop, J.; Kim, J. Y.; Lawrie, B. J.; Ahmadi, M.; Lee, B. R.; Kim, M.; Choi, S. J.; Kim, D. S.; Lee, M.; Lee, S. U.; Jo, Y.; Choi, H., Supramolecular design principles in pseudohalides for high-performance perovskite solar mini modules. *Joule* **2024,** *8* (8), 2283-2303.

17. Taylor, A. D.; Sun, Q.; Goetz, K. P.; An, Q. Z.; Schramm, T.; Hofstetter, Y.; Litterst, M.; Paulus, F.; Vaynzof, Y., A general approach to high-efficiency perovskite solar cells by any antisolvent. *Nat Commun* **2021,** *12* (1).

18. Hidalgo, J.; Atourki, L.; Li, R. P.; Castro-Méndez, A. F.; Kim, S.; Sherman, E. A.; Bieber, A. S.; Sher, M. J.; Nienhaus, L.; Perini, C. A. R.; Correa-Baena, J. P., Bulky cation hinders undesired secondary phases in FAPbI
perovskite solar cells. *Mater Today* **2023,** *68*, 13-21.

19. Kuai, L.; Li, J. N.; Li, Y. J.; Wang, Y. S.; Li, P. D.; Qin, Y. S.; Song, T.; Yang, Y. G.; Chen, Z. Y.; Gao, X. Y.; Sun, B. Q., Revealing Crystallization Dynamics and the Compositional Control Mechanism of 2D Perovskite Film Growth by In Situ Synchrotron-Based GIXRD. *Acs Energy Lett* **2020,** *5* (1), 8-+.

20. Perini, C. A. R.; Rojas-Gatjens, E.; Ravello, M.; Castro-Mendez, A. F.; Hidalgo, J.; An, Y.; Kim, S.; Lai, B.; Li, R. P.; Silva-Acuña, C.; Correa-Baena, J. P., Interface Reconstruction from Ruddlesden-Popper Structures Impacts Stability in Lead Halide Perovskite Solar Cells. *Adv Mater* **2022,** *34* (51).

21. Hope, M. A.; Nakamura, T.; Ahlawat, P.; Mishra, A.; Cordova, M.; Jahanbakhshi, F.; Mladenovic, M.; Runjhun, R.; Merten, L.; Hinderhofer, A.; Carlsen, B. I.; Kubicki, D. J.; Gershoni-Poranne, R.; Schneeberger, T.; Carbone, L. C.; Liu, Y. H.; Zakeeruddin, S. M.; Lewinski, J.; Hagfeldt, A.; Schreiber, F.; Rothlisberger, U.; Grätzel, M.; Milic, J. V.; Emsley, L., Nanoscale Phase Segregation in Supramolecular π-Templating for Hybrid Perovskite

Photovoltaics from NMR Crystallography. *J Am Chem Soc* **2021,** *143* (3), 1529-1538.

22. Zhao, X. M.; Ball, M. L.; Kakekhani, A.; Liu, T. R.; Rappe, A. M.; Loo, Y. L., A charge transfer framework that describes supramolecular interactions governing structure and properties of 2D perovskites. *Nat Commun* **2022,** *13* (1).

23. Wang, K.; Lin, Z. Y.; Zhang, Z. H.; Jin, L. R.; Ma, K.; Coffey, A. H.; Atapattu, H. R.; Gao, Y.; Park, J. Y.; Wei, Z. T.; Finkenauer, B. P.; Zhu, C. H.; Meng, X. E.; Chowdhury, S. N.; Chen, Z. Y.; Terlier, T.; Do, T. H.; Yao, Y.; Graham, K. R.; Boltasseva, A.; Guo, T. F.; Huang, L. B.; Gao, H. W.; Savoie, B. M.; Dou, L. T., Suppressing phase disproportionation in quasi-2D perovskite light-emitting diodes. *Nat Commun* **2023,** *14* (1).

24. Sanchez, S. L.; Tang, Y. P.; Hu, B.; Yang, J.; Ahmadi, M., Understanding the ligand-assisted reprecipitation of CsPbBr3 nanocrystals via high-throughput robotic synthesis approach. *Matter-Us* **2023,** *6* (9), 2900-2918.

25. Zhang, J. Y.; Wu, J. C.; Langner, S.; Zhao, B. L.; Xie, Z. Q.; Hauch, J. A.; Afify, H. A.; Barabash, A.; Luo, J. S.; Sytnyk, M.; Meng, W.; Zhang, K. C.; Liu, C.; Osvet, A.; Li, N.; Halik, M.; Heiss, W.; Zhao, Y. C.; Brabec, C. J., Exploring the Steric Hindrance of Alkylammonium Cations in the Structural Reconfiguration of Quasi-2D Perovskite Materials Using a High-throughput Experimental Platform. *Adv Funct Mater* **2022,** *32* (43).

26. Higgins, K.; Valleti, S. M.; Ziatdinov, M.; Kalinin, S. V.; Ahmadi, M., Chemical Robotics Enabled Exploration of Stability in Multicomponent Lead Halide Perovskites via Machine Learning. *Acs Energy Lett* **2020,** *5* (11), 3426-3436.

27. Higgins, K.; Ziatdinov, M.; Kalinin, S. V.; Ahmadi, M., High-Throughput Study of Antisolvents on the Stability of Multicomponent Metal Halide Perovskites through Robotics-Based Synthesis and Machine Learning Approaches. *J Am Chem Soc* **2021,** *143* (47), 19945-19955.

28. Yang, J.; Fuhr, A. S.; Roccapriore, K. M.; Dryzhakov, B.; Hu, B.; Sumpter, B. G.; Kalinin, S. V.; Ahmadi, M., Ligand-induced self-assembly of twisted two-dimensional halide perovskites. *ChemRxiv* **2024**.

29. Foadian, E.; Yang, J.; Harris, S. B.; Tang, Y.; Rouleau, C. M.; Joy, S.; Graham, K. R.; Lawrie, B. J.; Hu, B.; Ahmadi, M., Decoding the Broadband Emission of 2D Pb-Sn Halide Perovskites through High-Throughput Exploration. *Adv Funct Mater* **2024**, 2411164.

30. Song, H.; Yang, J.; Jeong, W. H.; Lee, J.; Lee, T. H.; Yoon, J. W.; Lee, H.; Ramadan, A. J.; Oliver, R. D. J.; Cho, S. C.; Lim, S. G.; Jang, J. W.; Yu, Z. K.; Oh, J. T.; Jung, E. D.; Song, M. H.; Park, S. H.; Durrant, J. R.; Snaith, H. J.; Lee, S. U.; Lee, B. R.; Choi, H., A Universal Perovskite Nanocrystal Ink for High-Performance Optoelectronic Devices. *Adv Mater* **2023,** *35* (8).

31. Lin, Y.; Fang, Y. J.; Zhao, J. J.; Shao, Y. C.; Stuard, S. J.; Nahid, M. M.; Ade, H.; Wang, Q.; Shield, J. E.; Zhou, N. H.; Moran, A. M.; Huang, J. S., Unveiling the operation mechanism of layered perovskite solar cells. *Nat Commun* **2019,** *10*.

32. Chen, S. S.; Xiao, X.; Chen, B.; Kelly, L. L.; Zhao, J. J.; Lin, Y. Z.; Toney, M. F.; Huang, J. S., Crystallization in one-step solution deposition of perovskite films: Upward or downward? *Sci Adv* **2021,** *7* (4).

33. Dubey, A.; Sanchez, S. L.; Yang, J.; Ahmadi, M., Lead-Free Halide Perovskites for Photocatalysis via High-Throughput Exploration. *Chemistry of Materials* **2024,** *36* (5), 2165-2176.

34. Chen, J. Y.; Zhai, Z. H.; Liu, Q.; Zhou, H. Q., The rise of quasi-2D Dion-Jacobson perovskites for photovoltaics. *Nanoscale Horiz* **2023,** *8* (12), 1628-1651.

35. Xiang, T.; Li, T.; Wang, M. S.; Zhang, W.; Ahmadi, M.; Wu, X. Y.; Xu, T. F.; Xiao, M. Q.; Xu, L.; Chen, P., 12-Crown-4 ether assisted in-situ grown perovskite crystals for ambient stable light emitting diodes. *Nano Energy* **2022,** *95*.

36. Chen, C. H.; Hsu, C. H.; Ni, I. C.; Lin, B. H.; Wu, C. I.; Kuo, C. C.; Chueh, C. C., Regulating the phase distribution of quasi-2D perovskites using a three-dimensional cyclic molecule toward improved light-emitting performance. *Nanoscale* **2022,** *14* (46), 17409-17417.

37. Peng, S.; Miao, Z.; Liang, Y.; Zhao, R.; Yuan, F.; Zhu, H.; Liang, W.; Shi, Y.; Li, P.; Zhang, Y.; Song, Y., Governing the dispersion of quasi-2D perovskite phases toward efficient and stable perovskite solar cells. *Matter-Us* **2024**.

38. Kong, L. M.; Zhang, X. Y.; Li, Y. G.; Wang, H. R.; Jiang, Y. Z.; Wang, S.; You, M. Q.; Zhang, C. X.; Zhang, T.; Kershaw, S. V.; Zheng, W. T.; Yang, Y. G.; Lin, Q. Q.; Yuan, M. J.; Rogach, A. L.; Yang, X. Y., Smoothing the energy transfer pathway in quasi-2D perovskite films using methanesulfonate leads to highly efficient light-emitting devices. *Nat Commun* **2021,** *12* (1).

39. Zhang, X.; Munir, R.; Xu, Z.; Liu, Y. C.; Tsai, H.; Nie, W. Y.; Li, J. B.; Niu, T. Q.; Smilgies, D. M.; Kanatzidis, M. G.; Mohite, A. D.; Zhao, K.; Amassian, A.; Liu, S. Z., Phase Transition Control for High Performance Ruddlesden-Popper Perovskite Solar Cells. *Adv Mater* **2018,** *30* (21).

40. Wang, Q.; Zheng, X. P.; Deng, Y. H.; Zhao, J. J.; Chen, Z. L.; Huang, J. S., Stabilizing the α-Phase of $CsPbI_3$ Perovskite by Sulfobetaine Zwitterions in One-Step Spin-Coating Films. *Joule* **2017,** *1* (2), 371-382.

41. Lafollette, D. K.; Hidalgo, J.; Allam, O.; Yang, J. H.; Shoemaker, A.; Li, R. P.; Lai, B. R. Y.; Lawrie, B.; Kalinin, S.; Perini, C. A. R.; Ahmadi, M.; Jang, S. S.; Correa-Baena, J.

P., Bromine Incorporation Affects Phase Transformations and Thermal Stability of Lead Halide Perovskites. *J Am Chem Soc* **2024**.

42. Yang, J.; LaFollette, D. K.; Lawrie, B. J.; Ievlev, A. V.; Liu, Y.; Kelley, K. P.; Kalinin, S. V.; Correa-Baena, J. P.; Ahmadi, M., Understanding the Role of Cesium on Chemical Complexity in Methylammonium-Free Metal Halide Perovskites. *Advanced Energy Materials* **2023,** *13* (33).

43. Ho, K.; Wei, M. Y.; Sargent, E. H.; Walker, G. C., Grain Transformation and Degradation Mechanism of Formamidinium and Cesium Lead Iodide Perovskite under Humidity and Light. *Acs Energy Lett* **2021,** *6* (3), 934-940.

44. Yu, S.; Yan, Y. J.; Abdellah, M.; Pullerits, T.; Zheng, K. B.; Liang, Z. Q., Nonconfinement Structure Revealed in Dion-Jacobson Type Quasi-2D Perovskite Expedites Interlayer Charge Transport. *Small* **2019,** *15* (49).

45. Wu, G. B.; Liu, T. H.; Hu, M. X.; Zhang, Z. P.; Li, S. L.; Xiao, L. G.; Guo, J.; Wang, Y. Y.; Zhu, A. N.; Li, W.; Zhou, H. Q.; Zhang, Y.; Chen, R. F.; Xing, G. C., Crystallinity and Phase Control in Formamidinium-Based Dion-Jacobson 2D Perovskite via Seed-Induced Growth for Efficient Photovoltaics. *Adv Mater* **2023,** *35* (36).

46. Guthrey, H.; Moseley, J., A Review and Perspective on Cathodoluminescence Analysis of Halide Perovskites. *Advanced Energy Materials* **2020,** *10* (26).

47. Deschler, F.; Price, M.; Pathak, S.; Klintberg, L. E.; Jarausch, D. D.; Higler, R.; Hüttner, S.; Leijtens, T.; Stranks, S. D.; Snaith, H. J.; Atatüre, M.; Phillips, R. T.; Friend, R. H., High Photoluminescence Efficiency and Optically Pumped Lasing in Solution-Processed Mixed Halide Perovskite Semiconductors. *J Phys Chem Lett* **2014,** *5* (8), 1421-1426.

48. Chen, H.; Maxwell, A.; Li, C. W.; Teale, S.; Chen, B.; Zhu, T.; Ugur, E.; Harrison, G.; Grater, L.; Wang, J. K.; Wang, Z. W.; Zeng, L. W.; Park, S. M.; Chen, L.; Serles, P.; Awni, R. A.; Subedi, B.; Zheng, X. P.; Xiao, C. X.; Podraza, N. J.; Filleter, T.; Liu, C.; Yang, Y.; Luther, J. M.; De Wolf, S.; Kanatzidis, M. G.; Yan, Y. F.; Sargent, E. H., Regulating surface potential maximizes voltage in all-perovskite tandems. *Nature* **2023,** *613* (7945), 676-+.